X-/γ-ray photon counting spectroscopy with an AlInP array

Article (Published Version)

Nuclear Inst. and Methods in Physics Research, A 1002 (2021) 165293

Contents lists available at ScienceDirect

Nuclear Inst. and Methods in Physics Research, A

journal homepage: www.elsevier.com/locate/nima

X-/γ-ray photon counting spectroscopy with an AlInP array

G. Lioliou [a,*], A.B. Krysa [b], A.M. Barnett [a]

[a] Space Research Group, School of Mathematical and Physical Sciences, University of Sussex, Falmer, Brighton, BN1 9QT, UK
[b] EPSRC National Epitaxy Facility, University of Sheffield, Mappin Street, Sheffield S1 3JD, UK

ARTICLE INFO

Keywords:
AlInP
X-ray spectroscopy
γ-ray spectroscopy
Pixel detector
Photodiode array

ABSTRACT

An AlInP 3 × 3 pixel monolithic array was fabricated from a p^+-i-n^+ structure wafer (6 μm thick i layer) grown by metalorganic vapour phase epitaxy; each pixel (square mesa photodiode) had an area of 200 μm × 200 μm. The pixels were initially electrically characterized and were then subjected to illumination by X-ray and γ-ray photons of energies ≤88 keV while each of them was in turn coupled to a custom-made, low noise, charge-sensitive preamplifier. The photon counting X-/γ-ray spectroscopic performance of the pixels was investigated by obtaining and analysing ^{55}Fe X-ray, ^{241}Am X-/γ-ray, and ^{109}Cd X-/γ-ray spectra; the energy resolution (Full Width at Half Maximum), when the array and preamplifier were operated at the maximum investigated temperature (100 °C), was 1.54 keV ± 0.08 keV at 5.9 keV, 1.58 keV ± 0.08 keV at 22.16 keV, and 1.57 keV ± 0.08 keV at 59.54 keV. This work sets the agenda for future development of an AlInP photon counting X-/γ-ray spectroscopic imager for uncooled operation in high temperature environments.

1. Introduction

X-ray and γ-ray spectroscopic imaging is used widely in space science, for example for astrophysical [1] and planetary [2] analysis. Terrestrial applications also benefit from spectroscopic X-/γ-ray imaging, including for health care [3], national security [4], and biosciences [5]. A critical component of every spectroscopic X-/γ-ray imager is the radiation detector.

X-/γ-ray detectors made of Si (e.g. CCDs [6] and DEPFETs [7]) have been common choices in such applications for photon energies $\lessapprox$ 10 keV as they are readily available and provide good energy resolutions when operated at temperatures <20 °C [8,9]. Detectors made of other materials have been developed for harder X-/γ-ray photons and operation in high temperature environments. High atomic number semiconductor detectors, e.g. Ge, $Cd_{1-x}Zn_xTe$, and GaAs [10–12], can provide better detection efficiencies at harder photon energies; at 60 keV the linear X-ray absorption coefficients are 9.45 cm^{-1} for Ge, 36.24 cm^{-1} for CdTe, and 9.54 cm^{-1} for GaAs [13], cf. 0.41 cm^{-1} for Si. In contrast to narrower bandgap, E_g, detectors such as Ge (E_g = 0.66 eV [14]) and Si (E_g = 1.12 eV [15]), wider bandgap semiconductor detectors such as $Cd_{1-x}Zn_xTe$ (E_g = 1.44 eV for CdTe [16]) and GaAs (E_g = 1.42 eV [17]) can be operated uncooled at temperatures ≥20 °C [10,12,18].

Other wide bandgap semiconductor detectors shown to be suitable for photon counting X-/γ-ray spectroscopy include $Al_{0.52}In_{0.48}P$ [19], $In_{0.5}Ga_{0.5}P$ [20], 4H-SiC [21], and diamond [22], of which $Al_{0.52}In_{0.48}P$ and $In_{0.5}Ga_{0.5}P$ also benefit from high atomic number. X-ray detection with $Al_{0.52}In_{0.48}P$ was first reported in 2016 [19,23,24]. The material benefits from a lattice match with GaAs, thus enabling epitaxial growth on readily available commercial substrates, as well as a linear absorption coefficient at moderate and hard photon energies larger than Ge and GaAs, e.g. 12.23 cm^{-1} at 60 keV, and an indirect bandgap of 2.31 eV [25], thus potentially providing both operation with high energy photons and at high temperatures. Single pixel $Al_{0.52}In_{0.48}P$ circular mesa p^+-i-n^+ photodiodes with 2 μm and 6 μm thick i layers have been reported to detect spectroscopically 5.9 keV X-ray photons at temperatures up to 100 °C [19,26] and they have been also investigated for their photon counting X-ray spectroscopic performance within the photon energy range 4.95 keV to 21.17 keV at more modest temperatures [27,28]. Whilst the early (2 μm thick) devices showed significant incomplete charge collection noise [27], improvement in the detector manufacture for the single pixel 6 μm thick i layer devices eliminated the behaviour [28].

In this article, growth, fabrication, and characterization of the first small (3 × 3, i.e. 9 pixel) monolithic $Al_{0.52}In_{0.48}P$ photodiode array is reported. The device had a p^+-i-n^+ structure (6 μm thick i layer) with pixels each of 200 μm × 200 μm area. All pixels were characterized at a temperature of 20 °C and one representative pixel was characterized at the temperature range 20 °C ≤ T ≤100 °C using ^{55}Fe, ^{241}Am, and ^{109}Cd radioisotope X-ray and γ-ray sources. It is the first time that $Al_{0.52}In_{0.48}P$ photodiode detectors in an array configuration have been investigated for photon counting X-/γ-ray spectroscopy and the first time that single pixel or array $Al_{0.52}In_{0.48}P$ detectors have been characterized at such high photon energies (up to 88 keV).

* Corresponding author.
E-mail address: G.Lioliou@sussex.ac.uk (G. Lioliou).

https://doi.org/10.1016/j.nima.2021.165293
Received 5 February 2021; Received in revised form 24 March 2021; Accepted 25 March 2021
Available online 29 March 2021

Table 1
Layer structure of the AlInP detector.

Material	Type	Dopant	Thickness (μm)	Doping density (cm^{-3})
GaAs	p^+	Zn	0.01	1×10^{19}
AlInP	p^+	Zn	0.2	5×10^{17}
AlInP	i	–	6	Nominally undoped
AlInP	n^+	Si	0.1	2×10^{18}
GaAs	n^+	Si	0.2	2×10^{18}
GaAs	n^+(substrate)	Si	350	2×10^{18}

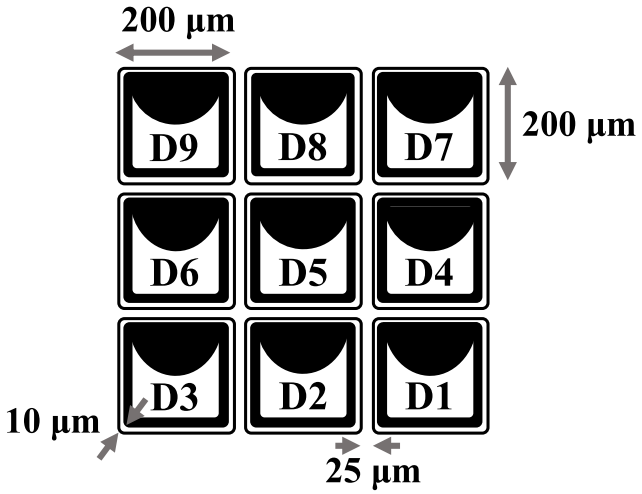

Fig. 1. Layout of the 3 × 3 AlInP pixel array (not to scale). The top Ohmic (quasi annular) contacts are shown in black. The pixel identification number (D1–D9), which is shown in the schematic, did not appear on the array.

2. Array structure

An $Al_{0.52}In_{0.48}P$ (herein after AlInP for simplicity) p^+-i-n^+ structure was grown by metalorganic vapour phase epitaxy (MOVPE) in a low pressure (150 Torr) horizontal reactor using hydrogen as a carrier gas. Trimethyl organometallic compounds, hydrides, disilane, and dimethylzinc:trimethylamine were used as precursors of groups III and V elements, and for n type and p type doping, correspondingly. The structure was grown on a commercial 2 inch (100) GaAs n^+ substrate with a misorientation of 10° towards ⟨111⟩A and a doping density of 2×10^{18} cm^{-3}. The layer structure is summarized in Table 1.

An AlInP 3 × 3 pixel array was formed from the epi-wafer by wet chemical etching; an H_3PO_4:H_2O_2:H_2O solution (at 1:1:1) was used followed by 10 s in an H_2SO_4:H_2O_2:H_2O (at 1:8:80) finishing etch solution. Square mesa diodes, each with 200 μm × 200 μm area and a 10 μm radius at each corner were formed. The distance between adjacent pixels was 25 μm. The top Ohmic contacts (20 nm Ti; 200 nm of Au) were of a quasi square annular design with an enlarged area bond pad. This shape, together with the highly doped p^+ top layer of the epitaxial structure, provided electric field uniformity across the pixel. Furthermore, the enlarged bond pad area facilitated wire bonding, and, compared to a planar contact, the quasi square annular provided lower contact coverage of the top face of each pixel (thus reducing the unwanted attenuation of photons). They covered 50% of the area of the pixels. The bottom Ohmic contact (20 nm InGe; 200 nm Au) was common for all pixels. The layout of the array is shown in Fig. 1.

The quantum detection efficiency, *QE*, of the AlInP pixels was calculated at photon energies from 1 keV to 100 keV using the Beer–Lambert law [29] and the accepted elemental mass absorption coefficients [13,30]. The p^+ layer and the whole of the i layer were assumed to be the only active layers; charge created by absorption of photons elsewhere in the structure (i.e. within the top Ohmic contacts and the GaAs p^+ contact layer) was considered to be lost. The results are shown in Fig. 2. The *QE* reduced from 0.5130 at 5.9 keV to 0.0026 at 88 keV for a fully depleted i layer. It should be noted here that the *QE* for a detector with a partially depleted i layer would be lower than that shown in Fig. 2.

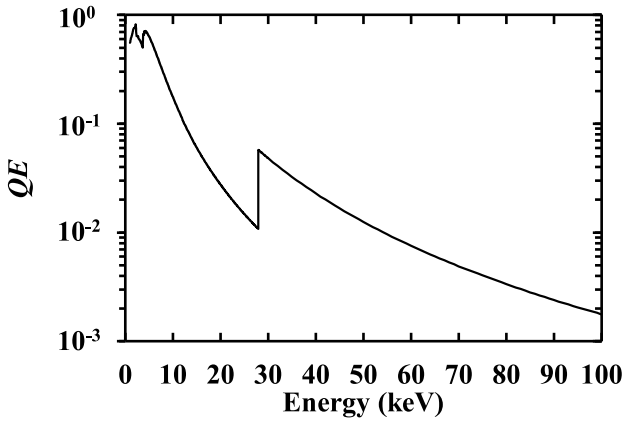

Fig. 2. Quantum detection efficiency of the AlInP pixels.

3. Electrical characterization

3.1. Dark current measurements

The leakage current of each pixel was measured as a function of applied reverse bias in order to quantify the white parallel noise contribution of each pixel to the achieved energy resolution of the spectrometer. Initially, the leakage current of all pixels was measured at 20 °C, followed by leakage current measurements of one pixel (D1) as functions of temperature (100 °C – 20 °C). The array was installed in an optically dark and electromagnetically shielded Al enclosure which was placed in a Temperature Applied Sciences Micro LT225 environmental test chamber [31] to enable control of the temperature. The dark currents of all pixels were measured, in turn, using a Keysight Technologies B2981 A Femto/Picoammeter [32], while a Keithley 2636B Source Measure Unit (SMU) [33] was used to apply the potential difference across each pixel. The SMU was connected to the bottom Ohmic contact (common for all pixels), while the Femto/Picoammeter was connected to the top Ohmic contact of the pixel studied; in each case, the top Ohmic contacts of the rest of the pixels not being investigated were not electrically connected to the Femto/Picoammeter. The leakage current of the TO–5 package of the array was also measured (as a function of bias and temperature) and separated from the total measured leakage current of the packaged pixels. The package leakage current was negligible at temperatures ≤60 °C.

The leakage current of all pixels as a function of applied reverse bias (up to −200 V) at 20 °C can be seen in Fig. 3. All the pixels, apart from D5 and D7, showed similar leakage currents; they ranged from 0.97 pA ± 0.01 pA (D1) to 11.33 pA ± 0.06 pA (D3) at −200 V applied reverse bias. The leakage current of D5 and D7 showed a more rapid increase with increased applied reverse bias compared to the rest of the pixels and hence the maximum applied reverse bias was limited to −70 V for D5 (105.7 pA ± 0.5 pA leakage current) and −45 V for D7 (320.5 pA ± 0.9 pA leakage current).

The leakage current of D1, measured up to −200 V applied reverse bias and within the temperature range 100 °C to 20 °C, is presented in Fig. 4(a). Here, the total leakage current of the packaged D1 is shown since the leakage current of the package also contributes to the noise of the spectrometer. The leakage current of the packaged pixel D1 reduced from 31.7 pA ± 0.2 pA at 100 °C to 0.99 pA ± 0.01 pA at 20 °C, at −200 V applied reverse bias. Assuming D1 had the intended epilayer structure and its i layer was fully depleted at −200 V (see Section 3.2),

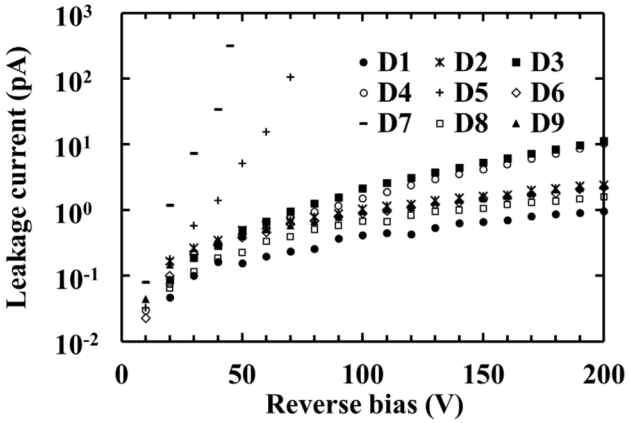

Fig. 3. Leakage current as a function of applied reverse bias for all pixels at 20 °C.

the internal electric field strength at this bias was 333 kV cm^{-1}, an extremely high value for a compound semiconductor detector [21].

Fig. 4(b) shows the leakage current of D1, excluding that of its package, as a function of temperature at three applied reverse biases. The leakage current density was 27.3 nA cm^{-2} ± 0.1 nA cm^{-2} at 100 °C and 2.48 nA cm^{-2} ± 0.03 nA cm^{-2} at 20 °C at the maximum investigated electric field strength (333 kV cm^{-1}, −200 V). The leakage current of 0.99 pA ± 0.01 pA (2.48 nA cm^{-2} ± 0.03 nA cm^{-2}) at 20 °C for D1 at this field strength is particularly impressive. The leakage current density of D1 at 100 °C was much smaller than that reported previously for high quality GaAs p$^+$-i-n$^+$ diodes (e.g. 1.937 μA cm^{-2} ± 0.008 μA cm^{-2} at only 50 kV cm^{-1} [34]). Comparable leakage current densities were measured with D1 and previously reported 4H-SiC devices with ultra-low leakage currents; 4H-SiC Schottky diodes had leakage current densities ranging from 0.1 pA cm^{-2} to 10 pA cm^{-2} at room temperature (25 °C) and −200 V (36 kV cm^{-1} electric field strength) [35], in comparison D1 exhibited 5 pA cm^{-2} leakage current density at the same electric field at 20 °C.

3.2. Capacitance measurements

The capacitances of the pixels were measured at up to −200 V applied reverse bias in order to extract important parameters of the pixels (depletion width and effective carrier concentration within the i layer) and to identify the white series noise contribution of each pixel to the achieved energy resolution of the spectrometer. Initially, the capacitances of only a subset of the pixels were measured at 20 °C (the subset, D1, D2, D3, D6, and D9, included at least one pixel of each row and of each column of the array). Capacitance measurements as functions of temperature (100 °C – 20 °C) of D1 followed. The array was installed in an enclosure similar to that used for the leakage current measurements and placed in the same environmental test chamber in order to control the temperature. The capacitance measurements were performed by a Hewlett-Packard 4275 A Multi Frequency LCR Meter [36] with a 50 mV rms magnitude and 1 MHz frequency test signal, while the bias was applied using a Keithley 6487 Picoammeter/Voltage Source [37]. The capacitance of the TO−5 package of the array was also measured (as a function of bias and temperature) and was separated from the total measured capacitance of the packaged pixels in order to extract the depletion layer capacitance. The uncertainty associated with a single measurement was estimated to be ± 0.1 pF, whereas the uncertainties associated with a set of measurements with no interconnections

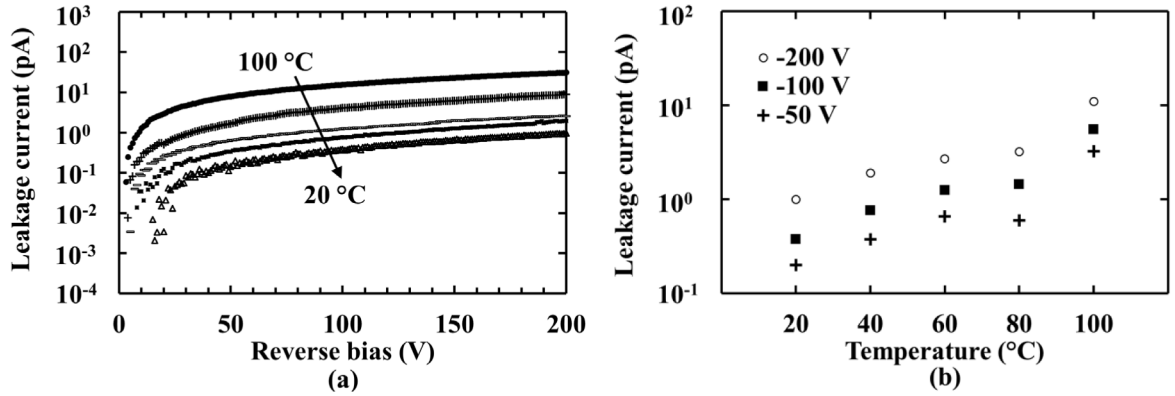

Fig. 4. Leakage current (a) of the packaged D1 up to −200 V applied reverse bias and (b) of D1 at −50 V, −100 V, and −200 V applied reverse bias, at temperatures between 100 °C and 20 °C. The error bars have been omitted; they are smaller than the symbol sizes.

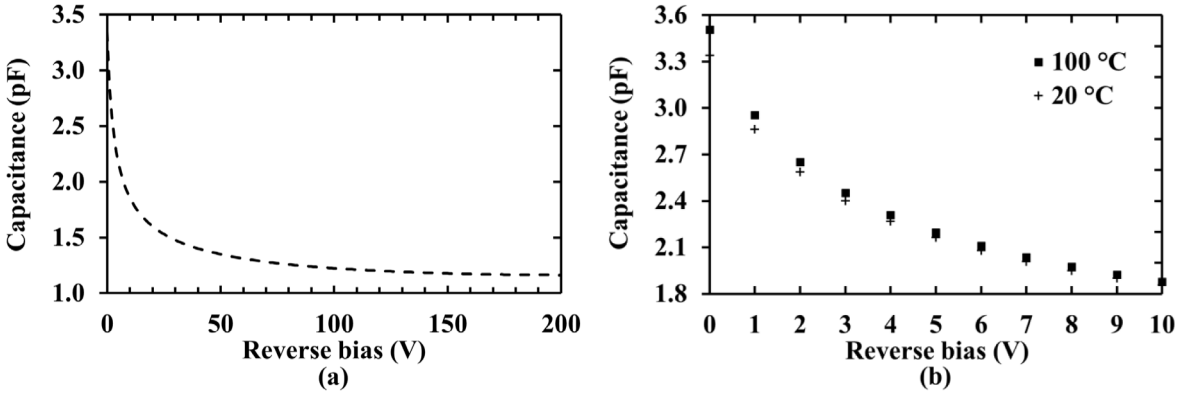

Fig. 5. Capacitance of D1, including the packaging capacitance, as a function of applied reverse bias, (a) at 20 °C (- - -) and (b) at 100 °C (■) and 20 °C (+).

changed was estimated to range between ± 0.005 pF and ± 0.009 pF (proportional to the value of the corresponding measured capacitance).

The capacitance of the packaged pixel D1 (i.e. including the packaging capacitance) as a function of applied reverse bias at 20 °C can be seen in Fig. 5(a). The mean capacitance among all the measured packaged pixels reduced from 3.37 pF ± 0.04 pF (rms error) at 0 V to 1.19 pF ± 0.02 pF (rms error) at −200 V applied reverse bias. The uncertainty associated with the mean of the measured capacitances (≤0.04 pF, rms error) was smaller than the measurement uncertainty of the capacitance measurements (± 0.1 pF), and thus, it can be said that all the investigated pixels had the same capacitance.

The capacitance of D1, including the packaging capacitance, as a function of reverse bias (only up to −10 V, for clarity), at the maximum (100 °C) and minimum (20 °C) measured temperature is shown in Fig. 5(b). At 100 °C, it reduced from 3.506 pF ± 0.008 pF to 1.177 pF ± 0.005 pF, when the magnitude of the applied reverse bias was increased from 0 V to −200 V. Similarly, at 20 °C, it reduced from 3.340 pF ± 0.008 pF to 1.169 pF ± 0.005 pF, when the magnitude of the applied reverse bias was increased from 0 V to −200 V.

The capacitance of the empty package was then subtracted from the total measured capacitance in order to investigate the temperature variation of the depletion layer capacitance of D1 and to extract the depletion layer width and the effective carrier concentration in the i layer. The depletion layer capacitance of D1 (which was equal to that of each of the other pixels, considering the uncertainties) at 0 V, −50 V, −100 V, and −200 V applied reverse bias, within the temperature range 100 °C to 20 °C, is presented in Fig. 6. The depletion layer capacitance with no externally applied bias reduced with decreasing temperature from 2.810 pF ± 0.009 pF at 100 °C to 2.657 pF ± 0.009 pF at 20 °C. However, the depletion layer capacitance remained unchanged as the temperature decreased from 100 °C to 20 °C, at applied reverse biases greater than (in magnitude) −50 V; it was 0.481 pF ± 0.007 pF at 100 °C and 0.487 pF ± 0.007 pF at 20 °C, at −200 V applied reverse bias. The temperature dependence of the depletion layer capacitance (and equally of the depletion layer width) at low applied reverse biases was explained by the possible presence of a thin region around the depletion layer with non-ionized dopants at low temperatures, which were ionized at high temperatures; the ratio of the thickness of this thin region over the thickness of the depletion layer was lower at high reverse biases compared to low reverse biases.

The depletion layer width of D1 (which was equal to that of each of the other pixels, considering the uncertainties) was extracted from the capacitance measurements (Fig. 6), assuming that D1 may be considered a parallel plate capacitor [14]. The depletion layer width of D1 at 20 °C can be seen in Fig. 7(a). It increased from 1.500 μm ± 0.005 μm at 0 V to 8.2 μm ± 0.1 μm at −200 V. Full depletion of D1 at 20 °C was achieved at −142 V applied reverse bias; the pixel was measured to have an 8 μm ± 2 μm depletion layer width, matching the intended i layer thickness (6 μm). The uncertainty in the depletion layer width was determined by combining the measurement uncertainties in the capacitance measurements (± 0.1 pF for a single measurement) and the Debye length. The Debye length, which is dependent upon the semiconductor material, its doping density, and the temperature [14], was calculated for AlInP with a doping concentration of 10^{15} cm^{-3} to reduce from 0.13 μm at 100 °C to 0.12 μm at 20 °C. The effective carrier concentration within the unintentionally doped i layer of D1 was calculated using the depletion layer capacitance and the differential capacitance profiling method [14]. When the doping within the i layer does not vary over distances less than a Debye length, the extracted effective carrier concentration represents the doping profile. The results of D1 at 20 °C is shown in Fig. 7(b). The minimum effective carrier concentration identified for D1 at 20 °C was 13×10^{14} cm^{-3} ± 3×10^{14} cm^{-3}. One of the possible reasons of this relatively high effective carrier concentration within the i layer could be a parasitic oxygen doping during the epitaxial process due to the strong affinity of Al to react with oxygen and forming oxygen-related defect states in the bandgap [38–40]. This prohibited the intrinsic layer being fully depleted at 0 V applied bias; an applied reverse bias of −142 V was required for full depletion of the i layer of D1 at 20 °C. Relatively high effective carrier concentration within the i layer (430×10^{14} cm^{-3} ± 70×10^{14} cm^{-3}) was also measured for 2 μm thick i layer AlInP p^+-i-n^+ photodiodes fabricated from a wafer grown by the same method as the one reported here [24].

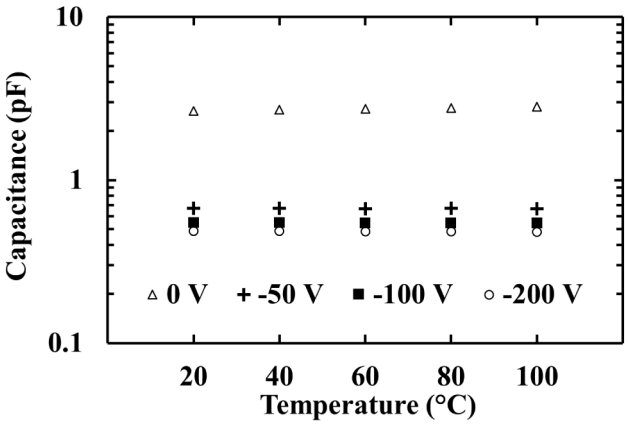

Fig. 6. Depletion layer capacitance of D1 as a function of temperature, at 0 V, −50 V, −100 V, and −200 V applied reverse bias.

4. X-ray and γ-ray spectroscopy

The radiation detection performance of the AlInP 3 × 3 pixel detector was investigated; three radioisotope sources, an ^{55}Fe X-ray source, an ^{241}Am X-ray and γ-ray source, and a ^{109}Cd X-ray and γ-ray source, were used to illuminate the pixel array. Initially, ^{55}Fe X-ray spectra were obtained with all nine pixels at a temperature of 20 °C. Following this, ^{55}Fe X-ray spectra were accumulated as functions of temperature (100 °C – 20 °C) with D1 to further investigate its X-ray detection performance; the spectral measurements, as functions of temperature, applied reverse bias, and shaping time, were accompanied by noise analysis in order to detangle the different noise contributions and to identify the dominant source of noise for the peak broadening. Finally, one of the pixels, D9, was subjected to illumination by all three radioisotope sources in turn (photon energies spanning from 5.9 keV to 88 keV): X-ray and γ-ray spectra were accumulated as functions of temperature (100 °C – 20 °C) at a single applied reverse bias and shaping time at each temperature.

Each pixel investigated was coupled to the input of a charge-sensitive preamplifier. The (single-channel) charge-sensitive preamplifier was custom-built, and had its feedback resistor and its external circuitry for preamplifier reset eliminated as per Ref. [41] in order to achieve lower noise in the preamplifier circuitry; the input transistor of the preamplifier was an InterFET 2N4416 Junction Field Effect Transistor (JFET) [42]. The connection between the input JFET and each pixel was such to ensure a slightly positive potential difference between its Gate and Source. Temperature control of the array-preamplifier assembly was, again, achieved using the same environmental test chamber. The output of the preamplifier was connected to an ORTEC 572 A shaping amplifier [43] (with selectable shaping times: 0.5 μs, 1 μs, 2 μs, 3 μs, 6 μs, and 10 μs) and the output of the shaping amplifier was connected to an ORTEC EASY-MCA−8K multichannel analyser (MCA) [44] for digitization; both instruments were kept at room temperature. The ^{55}Fe radioisotope X-ray source had an activity of 124 MBq; it was placed ≈ 8 mm above the top of the array. The ^{109}Cd radioisotope X-ray and γ-ray source had an activity of 285 MBq; it was placed 10 mm above the top of the array. The ^{241}Am radioisotope X-ray and γ-ray source had an activity of 299 MBq; it was placed 10 mm above the top of the array. Each source was encapsulated in its own stainless steel capsule

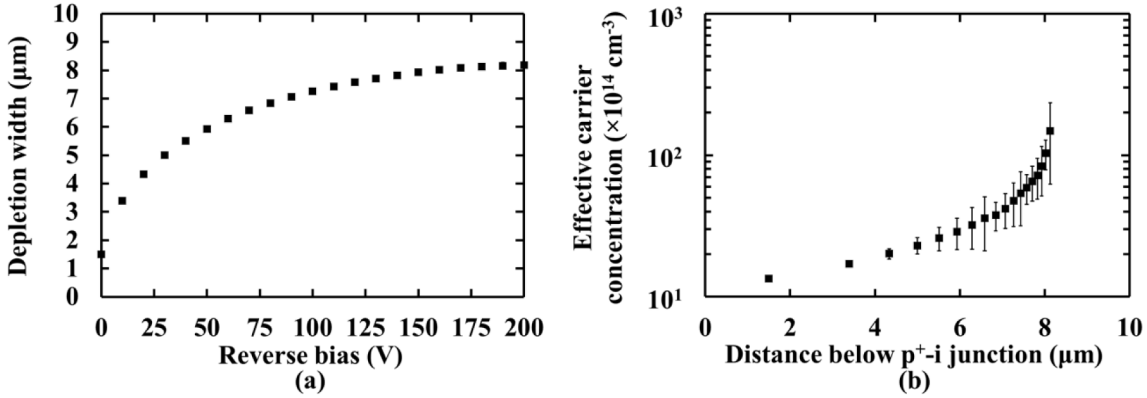

Fig. 7. (a) Depletion layer width as a function of applied reverse bias and (b) effective carrier concentration as a function of distance below the p^+-i junction of D1 at 20 °C. The error bars of the depletion width have been omitted; they are smaller than the symbol sizes.

with a 250 μm thick Be window. The characteristic emission lines of the ^{55}Fe radioisotope X-ray source [45], the ^{109}Cd radioisotope X-ray and γ-ray source [46], and the ^{241}Am radioisotope X-ray and γ-ray source [47,48], are summarized in Table 2.

4.1. ^{55}Fe X-ray spectra with all AlInP pixels at 20 °C

^{55}Fe X-ray spectra were accumulated at all available shaping times with the pixels and the preamplifier at a temperature of 20 °C at 0 V, −50 V, −100 V, and −200 V applied reverse bias. Exceptions were D5 and D7; for these two pixels applied reverse biases greater than (in magnitude) −50 V were not investigated due to the pixels' high leakage currents (see Fig. 3). The live time limit for each spectrum was 300 s; the dead time ranged between 1% and 4%.

An example ^{55}Fe X-ray spectrum, accumulated with D1, can be seen in Fig. 8. The main photopeak in each spectrum was the combination of the characteristic emissions of the radioisotope source: Mn Kα (at 5.9 keV) and Mn Kβ (at 6.49 keV) [45]. The combined Mn Kα and Kβ peaks were fitted with Gaussian peaks, accounting for the relative (Mn Kβ; Mn Kα) radioisotope X-ray source's emission ratio (=0.139 [45] when corrected for the slight difference in attenuation through 250 μm Be window of the source capsule) and quantum detection efficiency of the pixels (=0.849). The position (centroid MCA channel number) of the noise peak at 0 keV and the fitted Mn Kα peak at 5.9 keV were used to energy calibrate the MCA charge scale for each spectrum. The energy resolution, Full Width at Half Maximum (FWHM) at 5.9 keV, was recorded. The channel number of the low energy cut-off of the MCA was set appropriately (> 0 keV), after establishing the position of the noise peak at ≈ 0 keV, so that the counts of the noise peak were limited; part of the tail of the right hand side of the noise peak at ≈ 0 keV, was not entirely eliminated (e.g. see Fig. 8).

The low energy tailing of the ^{55}Fe X-ray photopeak (i.e. that at the left hand side of the photopeak) was attributed to partial collection of charge created in the non-active layers of the pixel. The valley-to-peak ratio, V/P, is an important performance figure of a spectrometer, quantifying the low energy tailing. This ratio was calculated by dividing the number of counts at the valley (3.5 keV) by the number of counts at the centroid channel number of the fitted Mn Kα Gaussian peak. The mean V/P among all the pixels ranged between 0.25 ± 0.04 (rms error) and 0.37 ± 0.05 (rms error) at 0 V, whereas it ranged between 0.04 ± 0.01 (rms error) and 0.07 ± 0.01 (rms error) at the rest of the applied reverse biases. The V/P values at applied reverse biases with a magnitude > 0 V were similar to those measured for previously reported AlInP detectors (0.048 and 0.058 for single pixel p^+-i-n^+ photodiodes with 6 μm thick i layer [49]) and GaAs detectors (from 0.02 to 0.09, with an average value of 0.04, for a 2 × 2 pixel array of square mesa p^+-i-n^+ photodiodes with 10 μm thick i layer [12]) at 20 °C. However, these values were not as good as the V/P values

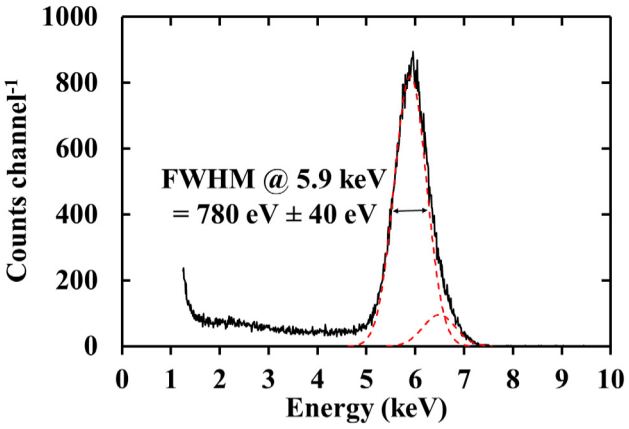

Fig. 8. ^{55}Fe X-ray spectrum (—) accumulated with the spectrometer pixel D1 (20 °C; −50 V; 3 μs). The fitted Mn Kα and Kβ peaks (---) are also visible.

achieved with Silicon drift diodes (SDDs) having integrated transistor and a Peltier cooler at 253 K; for those devices a value of 0.0001 was reached [50]. The increased number of counts at the energy range ≈ 1.5 keV to ≈ 3.5 keV, seen in Fig. 8, was attributed to the detector self-fluorescence of the Al K shell (Kα at 1.49 keV and Kβ at 1.56 keV), P K shell (Kα at 2.01 keV and Kβ at 2.14 keV), and In L shell (Lα at 3.28 keV).

The FWHM at 5.9 keV and the Equivalent Noise Charge (ENC) varied with shaping time and applied to the pixel reverse bias; this can be seen in Fig. 9 for D1. Similar trends were observed for all of the pixels. The energy resolution of the spectrometer pixel D1 improved with increased (in magnitude) applied reverse bias from 0 V to −50 V, and then stabilized up to and including the maximum applied reverse bias of −200 V. The best energy resolution achieved with D1 at 20 °C was 780 eV ± 40 eV FWHM at 5.9 keV (at 2 μs and 3 μs, and at applied reverse biases of −50 V, −100 V, and −200 V).

The best energy resolution achieved using pixels D1–D9 at −50 V applied reverse bias is presented in Fig. 10. This applied reverse bias was selected for comparison purposes since the maximum (in magnitude) reverse bias applied to D5 and D7 was −50 V, and the energy resolution achieved with the rest of the pixels did not change for an increase in magnitude of applied reverse bias beyond −50 V. All pixels (apart from D7) had the same energy resolution, within uncertainties, at 20 °C, despite the slight variations of their leakage current. The FWHM at 5.9 keV (excluding that achieved with D7) ranged from a low (best) of 780 eV ± 40 eV, for D1, D3, and D4, to a high (worst) of 810 eV ± 40 eV for D5, with a mean FWHM at 5.9 keV of 790 eV ± 10 eV. The best energy resolution achieved with the

Table 2
Characteristic emission lines and their corresponding energies and intensities, *I*, (photons per 100 disintegrations), of the three radioisotope X-ray and γ-ray sources used [45–48].

^{55}Fe X-ray			^{109}Cd X-ray and γ-ray			^{241}Am X-ray and γ-ray		
Char. emissions	Energy (keV)	*I* %	Char. emissions	Energy (keV)	*I* %	Char. emissions	Energy (keV)	*I* %
Mn Kα	5.9	24.57	Ag Lα	2.98	10.4	Np $L\alpha_2$	13.76	1.22
Mn Kβ	6.49	3.389	Ag $K\alpha_2$	21.99	29.2	Np $L\alpha_1$	13.95	11.4
			Ag $K\alpha_1$	22.16	55.1	Np Lβ	16.11–17.99	18.6
			Ag Kβ	24.9	17.92	Np Lγ	20.78–21.49	4.276
			γ-ray	88	3.65	γ-ray	26.3	2.31
						γ-ray	33.2	0.1215
						γ-ray	43.4	0.0669
						γ-ray	59.54	35.92

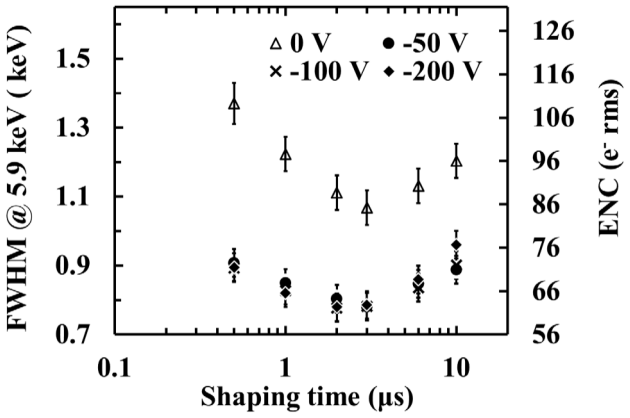

Fig. 9. FWHM at 5.9 keV (Mn Kα) and ENC of the spectrometer pixel D1, within the investigated shaping time range, at 0 V, −50 V, −100 V, and −200 V applied reverse bias, at 20 °C. The uncertainties of the FWHM at 5.9 keV, shown in the figure by the error bars, were related to the Gaussian fitting of the photopeak and ranged between ± 40 eV and ± 60 eV.

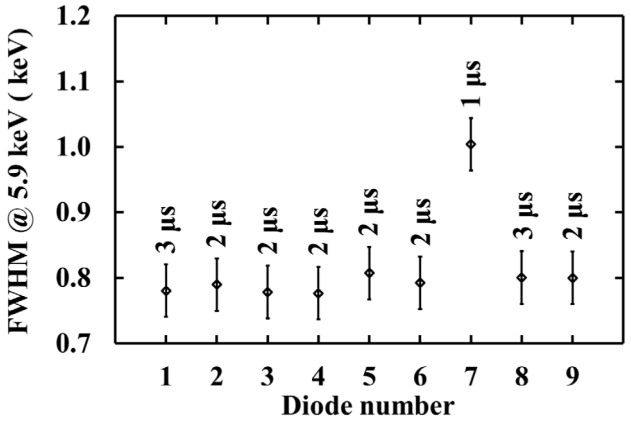

Fig. 10. The best energy resolution (FWHM at 5.9 keV) achieved using each pixel at 20 °C, at −50 V applied reverse bias.

pixel D7 based spectrometer was poorer (1000 eV ± 40 eV FWHM at 5.9 keV) compared to that achieved with the rest of the pixels. This was attributed to that pixel having much higher leakage current cf. the other pixels (see Fig. 3). The energy resolution of the spectrometer using each of the pixels (apart from D7) was notably better compared to what had been previously achieved using earlier circular mesa AlInP photodiode detectors of a similar size and coupled to similar electronics (at 20 °C in each case); for those earlier devices 900 eV FWHM at 5.9 keV was achieved with a 2 μm i layer AlInP p^+-i-n^+ circular photodiode with 200 μm diameter [19] and 850 eV FWHM at 5.9 keV with a 6 μm i layer AlInP p^+-i-n^+ circular photodiode with 217 μm ± 15 μm diameter [26].

Even though the energy resolution (FWHM at 5.9 keV) of the reported spectrometers did not improve with increased (in magnitude) applied reverse bias beyond −50 V, an increased applied reverse bias (electric field) may have improved the charge transport within the active layer of the corresponding pixel, resulting in reduced charge trapping/recombination. Whilst a reduction in the noise associated with charge trapping/recombination leads to a clear improvement in energy resolution when the reduction in that noise is large compared with the other noises in the system, when the charge trapping/recombination noise reduction is relatively small (typically by consequence of the noise being small in absolute terms to begin with) an overall reduction in FWHM is not apparent. As such, analysis was conducted to investigate the potential improvement of the charge transport and charge collection of the pixels with increased (in magnitude) applied reverse bias by other methods.

In a detector which is not fully depleted at its lowest operating reverse bias and where the thickness of the depletion layer is not great enough to ensure complete absorption of all photons at a given energy, the total number of counts within a peak in the spectrum corresponding to those photons (the fitted Mn Kα, at 5.9 keV, Gaussian peak in the present case) would be expected to increase as a function of increased (in magnitude) applied reverse bias, as a result of the increased thickness of the depletion layer, and as per the Beer–Lambert law and the specific variation of the depletion layer thickness with applied reverse bias. In situations where the charge collection efficiency is less than unity, improved charge transport may further increase the number of counts contributing to the peak (again the fitted Mn Kα, at 5.9 keV, Gaussian peak in the present instance).

Given this, the total number of counts within the fitted Mn Kα (at 5.9 keV) Gaussian peak was recorded for all spectra accumulated at 20 °C. Proceeding on the basis that any variation in the quality of the epitaxial material across the relatively small area of the array would be negligible, the mean value (across all investigated shaping times) of the total number of counts for each pixel at each applied reverse bias was then calculated. This was then used to compute the mean value of the total number of counts within the fitted Mn Kα Gaussian peak across all pixels; this is presented in Fig. 11. It increased from 2.1×10^4 $\pm 0.3 \times 10^4$ (rms error) at no applied bias to $9 \times 10^5 \pm 1 \times 10^5$ (rms error) at −200 V applied reverse bias. The number of counts expected to be detected within the Mn Kα photopeak at each applied reverse bias, based on the change of depletion layer thickness (relative to that at −200 V) and excluding any changes in charge trapping/recombination, is also shown in Fig. 11. Comparisons between the two data series suggested that the increase of the total number of counts within the fitted Mn Kα Gaussian peak as the applied reverse bias was increased beyond −50 V (at 20 °C) was attributable solely to the increase of the depletion width and not to reductions in charge trapping/recombination. However, incomplete charge collection/recombination was detected when the pixels were operated at 0 V applied bias; improved charge transport at −50 V applied reverse bias compared to that at no applied bias was found.

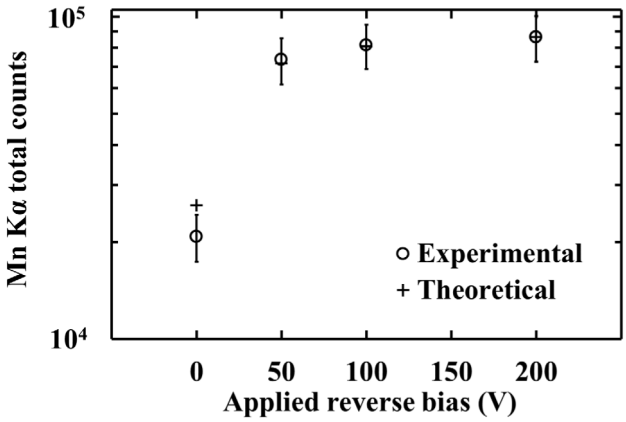

Fig. 11. Experimental mean across all pixels (○) and theoretical (+) total number of counts within the Mn Kα (at 5.9 keV) Gaussian peak, as a function of applied reverse bias.

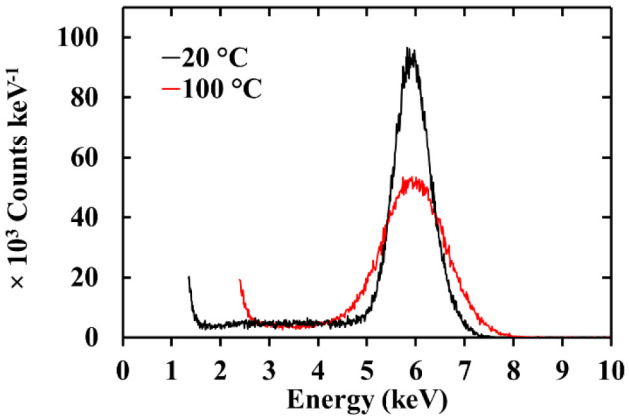

Fig. 12. ^{55}Fe X-ray spectra obtained with the spectrometer pixel D1 at 100 °C (−100 V; 0.5 μs; 1.49 keV ± 0.06 keV FWHM at 5.9 keV; —) and at 20 °C (−100 V; 2 μs; 0.82 keV ± 0.04 keV FWHM at 5.9 keV; —). The count rate within the fitted Mn Kα (at 5.9 keV) Gaussian peak was the same for both spectra.

4.2. Temperature dependent ^{55}Fe X-ray spectra with D1: noise analysis

^{55}Fe X-ray spectra were then accumulated with the spectrometer pixel D1 as functions of temperature (100 °C – 20 °C) using the same range of applied reverse biases and shaping times, live time limit, and MCA charge scale energy calibration and analysis procedure as per Section 4.1. The dead time of the spectroscopic system ranged between 1% and 10%, within the investigated temperatures.

The spectra with the settings (applied reverse bias and shaping time) which gave the lowest FWHM at 5.9 keV (i.e. best energy resolution) at 100 °C and 20 °C are shown in Fig. 12. The detected count rate within the fitted Mn Kα (at 5.9 keV) Gaussian peak was the same at both spectra; it was found to be 254 counts s^{-1} ± 16 counts s^{-1} at 100 °C and 259 counts s^{-1} ± 16 counts s^{-1} at 20 °C. The energy resolution improved as the temperature decreased from 100 °C (1.49 keV ± 0.06 keV FWHM at 5.9 keV) to 20 °C (0.82 keV ± 0.04 keV FWHM at 5.9 keV). The V/P was calculated for all the spectra, as per Section 4.1. The mean V/P across the investigated shaping times, at each applied reverse bias and temperature, was then computed. The mean V/P reduced from 0.70 ± 0.06 at 100 °C to 0.36 ± 0.06 at 20 °C at 0 V, from 0.2 ± 0.1 at 100 °C to 0.06 ± 0.03 at 20 °C at −50 V, and from 0.2 ± 0.1 at 100 °C to 0.05 ± 0.01 at 20 °C at −100 V and −200 V applied reverse bias. These results suggested that the V/P improvement broadly followed the energy resolution improvement, similar to previous reports [12], in which the V/P achieved with a pixel from a 2 × 2 pixel array (square mesa p^+-i-n^+ photodiodes with 10 μm thick i layer) improved from 0.10 at 100 °C to 0.02 at 20 °C.

The energy resolution (FWHM at 5.9 keV) achieved with the spectrometer pixel D1 within the range of investigated shaping times, at all applied reverse biases and temperatures, is shown in Fig. 13. The energy resolution improvement with reducing temperature is highlighted in Fig. 13; the y-axis for all parts of Fig. 13, ranged from 0.7 keV (56 e^- rms) to 2.9 keV (231 e^- rms). As was the case at 20 °C, the energy resolution at all temperatures improved as the magnitude of the applied reverse bias was increased up to −50 V, whereas it remained unchanged (within uncertainties) for up to (and including) −200 V. The optimum available shaping time, defined as the shaping time corresponding to the best FWHM at 5.9 keV, lengthened with decreasing temperature, from 0.5 μs at 100 °C to 2 μs at 20 °C. Both of these observations, based on Fig. 13, are discussed in the noise analysis section, which follows.

The energy resolution of a non-avalanche photodiode based photon counting X-ray spectrometer is defined by the quadratic sum of three (independent) terms; the Fano noise, the incomplete charge collection noise, and the electronic noise [51]. The Fano noise and the incomplete charge collection noise are both photon energy dependent; the former arises due to the statistical nature of the ionization process [52], whereas the latter results from charge carrier trapping and recombination due to crystal imperfections [53]. The electronic noise does not depend on the energy of the photons; it is composed of the white series (*WS*) noise (including the induced gate current noise), the white parallel (*WP*) noise, the $1/f$ noise, and the dielectric noise (*DN*) [51].

The Fano noise, the incomplete charge collection noise, and part of the electronic noise ($1/f$ noise and dielectric noise) are all shaping time invariant contributions. However, the white series noise, depending on the total capacitance (i.e. including the capacitances of the pixel, the package, and the input JFET, as well as the feedback, the stray, and, if present, the test capacitance) is inversely proportional to the shaping time and the white parallel noise, depending on the total leakage current (leakage current of the pixel, its package, and the input JFET) is proportional to the shaping time. The shaping time where the quadratic sum of the white series and the white parallel noise is minimized, is the optimum shaping time i.e. that at which the best energy resolution is achieved at a given temperature and applied reverse bias. The optimum shaping time (which is determined as above) and the optimum available shaping time (which is determined from the above and the shaping times selectable on a shaping amplifier) are not necessarily identical if the shaping amplifier cannot be infinitely continuously (cf. discretely) adjusted. The equivalent noise charge, in e^- rms, can thus be expressed as

$$N^2 = A\frac{1}{\tau} + B\tau + C \tag{1}$$

where A represents the white series noise contribution, B represents the white parallel noise contribution, and C represents the rest of the noise contributions [54]; A, B, and C can be estimated from a multidimensional least squares fitting of the measured noise as a function of shaping time. Hence, the equivalent total capacitance and total leakage current in the spectroscopic system which give rise to the photopeak broadening can be estimated. The quadratic sum of the white series and the white parallel noise is minimized at the shaping time (optimum shaping time, τ_{opt}) where the white series noise $\left(A\frac{1}{\tau_{opt}}\right)$ and the white parallel noise ($B\tau_{opt}$) are equal, hence, the optimum shaping time,

$$\tau_{opt} = \sqrt{\frac{A}{B}}. \tag{2}$$

To further detangle the shaping time invariant noise contributions, the Fano and the $1/f$ noise were computed and then subtracted (in quadrature) from the shaping time invariant contribution, to give the quadratic sum of the dielectric noise and, if any, the incomplete charge collection noise. The Fano noise at 5.9 keV was computed considering a Fano factor of 0.12 (since the Fano factor of AlInP is yet to

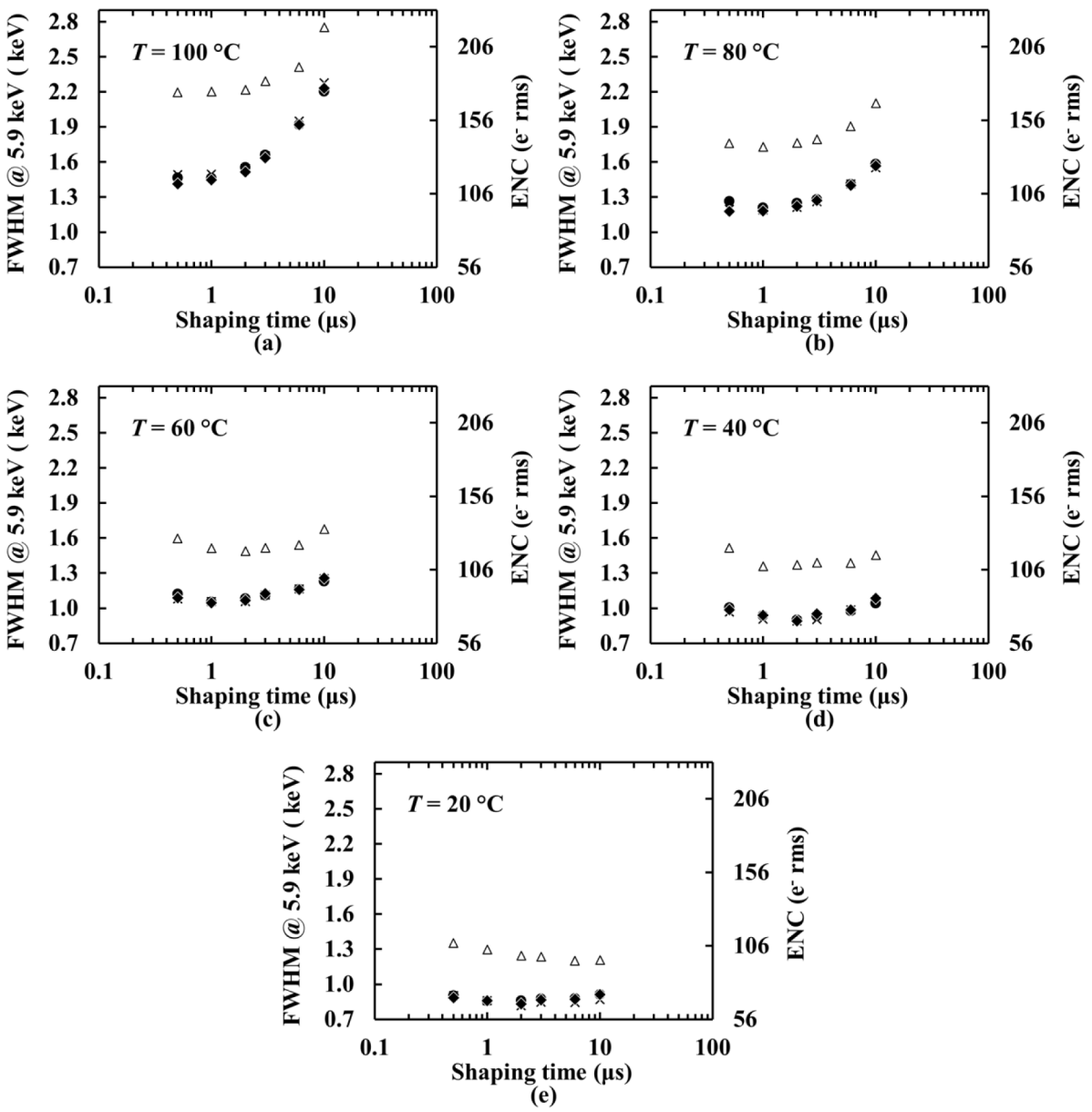

Fig. 13. Energy resolution (FWHM at 5.9 keV) and ENC within the investigated shaping time range at 0 V (△), −50 V (●), −100 V (×), and −200 V (◆) applied reverse bias with the D1-preamplifier system subjected to temperatures of (a) 100 °C; (b) 80 °C; (c) 60 °C; (d) 40; and (e) 20 °C.

be determined, that of GaAs [17], another wide bandgap material, was used) and an electron hole pair creation energy with a temperature dependency of, $\omega(T) = 6.31-0.0033T$ [55]. The $1/f$ noise was computed using the total capacitance estimated from the multidimensional nonlinear fitting; at all investigated temperatures, it was <5 e^- rms [51].

The multidimensional nonlinear least squares fitting of the FWHM at 5.9 keV as a function of shaping time Eq. (1) at 100 °C and 20 °C can be seen in Fig. 14. The experimental data points at −100 V applied reverse bias are presented in Fig. 14, but the same performance was observed at −50 V and −200 V applied reverse bias (Fig. 13). The calculated Fano noise, as well as the estimated white series (*WS*) noise, white parallel (*WP*) noise, and the quadratic sum of the dielectric and, if any, incomplete charge collection (*DN* & *ICC*) noise, are also shown in Fig. 14. Incomplete charge collection/recombination was previously show to be insignificant at 20 °C and applied reverse biases −50 V and greater in magnitude (see Section 4.1; nevertheless, *ICC* is known to be temperature dependent and thus at this stage cannot be excluded at all temperatures. The optimum shaping time was calculated at each temperature using Eq. (2), and was found to be 0.8 µs at 100 °C and 2.8 µs at 20 °C. However, due to the limited availability of the shaping times, the optimum available shaping time was 0.5 µs at 100 °C and between 2 µs (0.82 keV ± 0.04 keV FWHM at 5.9 keV) and 3 µs (0.85 keV ± 0.04 keV FWHM at 5.9 keV) at 20 °C.

The dominant source of noise at 100 °C and −100 V applied reverse bias (as well as −50 V and −200 V) was identified as a function of shaping time; it was the combined contribution (summed in quadrature) of the dielectric and (if any) incomplete charge collection noise at ≤4 µs and the white parallel noise, arising from 217 pA ± 6 pA total leakage current (uncertainty propagated from the nonlinear least squares fitting) at > 4 µs. The white parallel noise at 20 °C and −100 V applied reverse bias (and −50 V and −200 V) was minimal; it arose from only 6 pA ± 2 pA total leakage current, and thus the dominant source of noise across the shaping times investigated at 20 °C was the combined contribution (summed in quadrature) of the dielectric and (if any) incomplete charge collection noise. The quadratic sum of the dielectric and incomplete charge collection noise was calculated at all temperatures and all applied reverse biases; the calculated quadratic

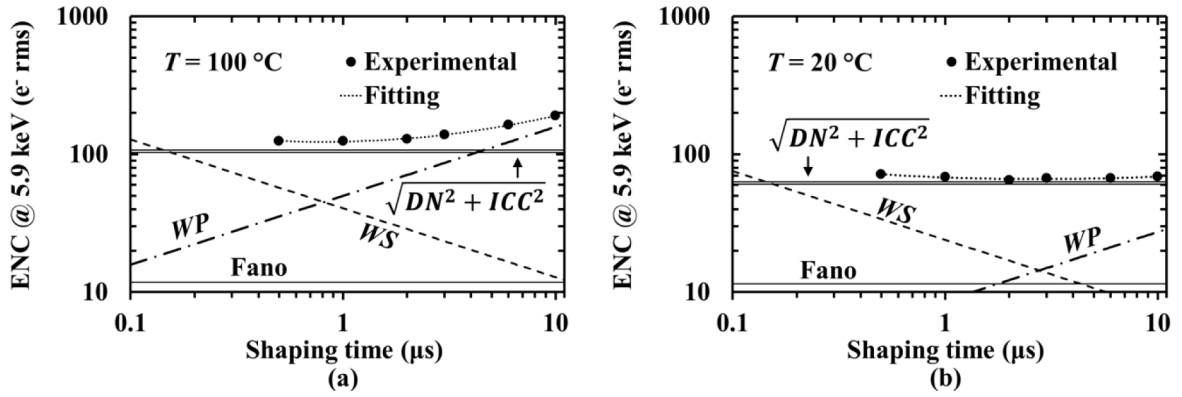

Fig. 14. Measured ENC at Mn Kα (5.9 keV) (●) and extracted noise contributions (white parallel noise (*WP*, ···), white series noise (*WS*, - - -), Fano noise (—), and quadratic sum of the dielectric and incomplete charge collection noise (*DN* & *ICC*, =) from a multidimensional least squares fitting of the experimental points (···), at (a) 100 °C and (b) 20 °C. The $1/f$ noise contribution was <5 e^- rms in both cases and is excluded from the figure.

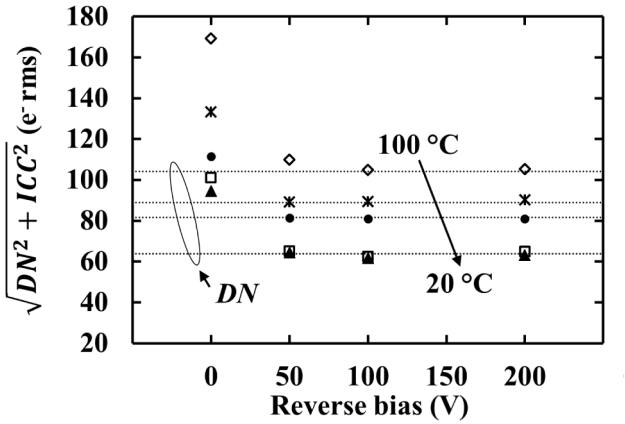

Fig. 15. Equivalent noise charge of the quadratic sum of the dielectric and incomplete charge collection noise as a function of applied reverse bias and across the investigated temperature range for the spectrometer pixel D1. The lines of best fit (···), calculated using linear least squares fitting, of the quadratic sum of the dielectric and incomplete charge collection noise as a function of applied reverse bias at applied reverse biases which only the dielectric noise was present (i.e. corresponding to the dielectric noise contribution) at each temperatures, are also shown.

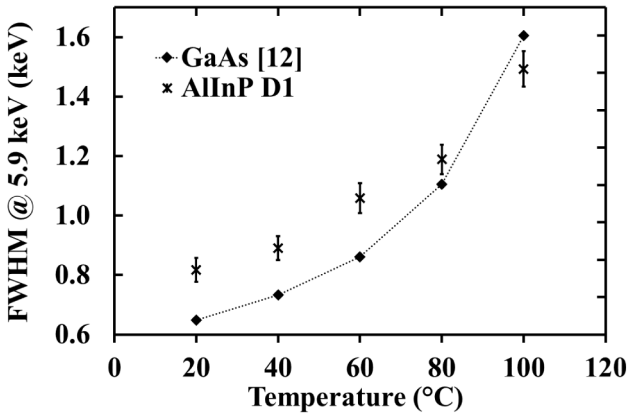

Fig. 16. Best energy resolution (lowest FWHM at 5.9 keV) achieved with the spectrometer pixel D1 at −100 V and the previously published GaAs pixel based spectrometer [12], within the temperature range 100 °C to 20 °C. The dotted line is a guide for the eye only.

sum of the Fano and $1/f$ noise was subtracted in quadrature from the shaping time invariant noise contribution determined from the multidimensional nonlinear fittings (Eq. (1)). This is shown as a function of applied reverse bias, at all investigated temperatures, in Fig. 15.

The quadratic sum of the dielectric and incomplete charge collection noise reduced with increased (in magnitude) applied reverse bias and then remained stable for further applied reverse bias increase, at each temperature. Although the capacitance of D1 (and its dielectric noise contribution) reduced with increased (in magnitude) applied reverse bias (Fig. 5), the reduction of the quadratic sum of the dielectric and incomplete charge collection noise with increased (in magnitude) applied reverse bias was mainly attributed to the reduction of the incomplete charge collection noise. There was no improvement in the quadratic sum of the dielectric and (if any) incomplete charge collection noise for increased (in magnitude) applied reverse biases > −100 V at 100 °C and > −50 V at the rest of the temperatures. Thus, it was concluded that the incomplete charge collection noise was insignificant for applied reverse biases > −100 V at 100 °C and > −50 V at the rest of the temperatures, and that only the dielectric noise contributed to the quadratic sum of the dielectric and incomplete charge collection noise under these conditions. This indicates that incomplete charge collection noise was greater at high temperatures, which was consistent with expectations [8]; the charge collection noise contribution increases with decreasing charge collection efficiency [56], with the latter deteriorating at increased temperatures [57]. The dielectric noise at each temperature was calculated by finding the line of best fit, using linear least squares fitting, of the dielectric noise as a function of applied reverse bias (at which only the dielectric noise was present) at each temperature. The dielectric noise reduced from 104 e^- rms at 100 °C to 64 e^- rms at 40 °C and 20 °C. In addition to the dielectric noise from the detector itself and its packaging, sources of dielectric noise were the feedback capacitance, the input JFET itself (dielectrics, passivation) and its packaging, and any other unknown lossy dielectrics at the input of the preamplifier [54,58,59]. An appropriate redesign of the preamplifier front-end would thus reduce the dielectric noise contribution and advance the noise performance of the reported spectrometer.

The best FWHM at 5.9 keV achieved at −100 V (equal to those at −50 V and −200 V, within uncertainties) as a function of temperature can be seen in Fig. 16. The values achieved using a GaAs pixel spectrometer of a similar design [12] are also presented for comparison. The AlInP pixel spectrometer had better energy resolution than the similar GaAs instrument at 100 °C, whereas the opposite was the case at temperatures ≤80 °C. The best (smallest) FWHM at 5.9 keV at 100 °C were 1.49 keV ± 0.06 keV for the AlInP instrument and 1.61 keV ± 0.04 keV for the GaAs instrument [12].

It is interesting to compare the equivalent noise charge present in each system as a function of temperature. For the AlInP instrument, the total noise reduced from 125 e^- rms ± 5 e^- rms at 100 °C to 65 e^- rms ± 3 e^- rms at 20 °C, for the GaAs instrument the total noise

reduces from 166 e^- rms ± 4 e^- rms at 100 °C to 66 e^- rms ± 2 e^- rms at 20 °C. Although similar quantities of noise were present in both spectrometers at 20 °C, the AlInP instrument had lower noise at 100 °C. This was mainly attributable to the lower leakage current of the AlInP pixel, highlighting the beneficial effect of wider bandgaps on the noise at high temperatures. On the other hand, the FWHM at 5.9 keV (in energy terms) achieved at 20 °C using the AlInP instrument was poorer than that achieved with the GaAs instrument, despite them having similar equivalent noise charge, due to the larger electron–hole pair creation energy of AlInP cf. GaAs. The results in Fig. 16 highlight the importance of tailoring detectors to the specific temperature regime expected to be encountered, rather than relying on a single technology to be a panacea.

Although the AlInP spectrometer had better energy resolution (FWHM at 5.9 keV) at 100 °C than the similar GaAs instrument, they both had inferior energy resolutions compared to the best experimental results achieved with a single pixel 4H-SiC detector (233 eV FWHM at 5.9 keV [21]). However, the 4H-SiC detector was coupled to ultra low-noise preamplifier electronics of a substantially different design than was used for the AlInP and GaAs instruments and thus the results are not directly comparable.

4.3. Temperature dependent X-ray and γ-ray spectroscopy

^{55}Fe X-ray, ^{241}Am X-ray and γ-ray, and ^{109}Cd X-ray and γ-ray spectra were then obtained across the same temperature range using one representative pixel, D9. The pixel D9 had the same performance as the rest of the pixels in terms of its same capacitance (see Section 3.2) and best FWHM at 5.9 keV at 20 °C (Fig. 10, with the exception of D7), while its leakage current was neither the highest nor the lowest measured among all the pixels (Fig. 3). Additionally, pixel D9 was at the diagonally opposite corner of the array to D1 (Fig. 1), the pixel that was chosen for the noise analysis of the spectroscopic system presented in Section 4.2, thus providing the greatest possible physical separation between the two pixels investigated in this way and hence taking advantage of the full size of the array. One spectrum was obtained at each temperature with each radioisotope source; −100 V applied reverse bias was selected since the FWHM at 5.9 keV was found to be independent of bias beyond −50 V (Figs. 8 and 13) and the increase of depletion layer width beyond −100 V was minimal (Fig. 11). The optimum available shaping time (as identified from the measurements using the radioisotope ^{55}Fe X-ray source presented in Section 4.2) was selected for each temperature; 0.5 μs at 100 °C, 1 μs at 80 °C, and 2 μs at 60 °C, 40 °C, and 20 °C. The live time of the spectra obtained with each radioisotope source was adjusted to reflect the different activities and emission characteristics of the sources, as well as the different quantum detection efficiency of D9 at the corresponding energies. The live time limit was 300 s for the ^{55}Fe X-ray spectra, and 8 h for the ^{241}Am and ^{109}Cd X-ray and γ-ray spectra. One additional ^{109}Cd X-ray and γ-ray spectrum with a live time limit of 72 h was accumulated at 20 °C for the 88 keV γ-ray photopeak to have sufficient counts. While the dead time of the spectroscopic system accumulating the ^{55}Fe X-ray spectra within the investigated temperature range varied between 1% and 10%, the dead time of the ^{241}Am and ^{109}Cd X-ray and γ-ray spectra remained <1%.

The MCA charge scale energy calibration and the analysis of the ^{55}Fe X-spectra was performed as described in Section 4.1; the spectra obtained at the maximum and at the minimum temperature are shown in Fig. 17. The energy resolution (FWHM at 5.9 keV) for the spectrometer pixel D9 improved with decreasing temperature from 1.54 keV ± 0.08 keV (100 °C) to 0.88 keV ± 0.04 keV (20 °C). Within uncertainties, the energy resolutions achieved with D9 were the same as those using D1 (shown in Fig. 12; 1.49 keV ± 0.06 keV at 100 °C and 0.82 keV ± 0.04 keV at 20 °C).

The ^{241}Am X-ray and γ-ray spectra accumulated at 100 °C and 20 °C using the spectrometer pixel D9 are presented in Fig. 18. A Gaussian

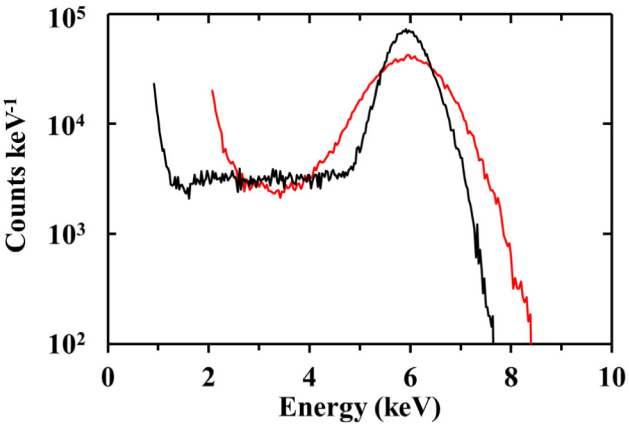

Fig. 17. ^{55}Fe X-ray spectra obtained with the spectrometer pixel D9 at 100 °C (−100 V; 0.5 μs; 1.54 keV ± 0.08 keV FWHM at 5.9 keV; —) and at 20 °C (−100 V; 2 μs; 0.88 keV ± 0.04 keV FWHM at 5.9 keV; —). The photopeak is the combination of the characteristic Mn Kα and Mn Kβ photons from the ^{55}Fe radioisotope X-ray source.

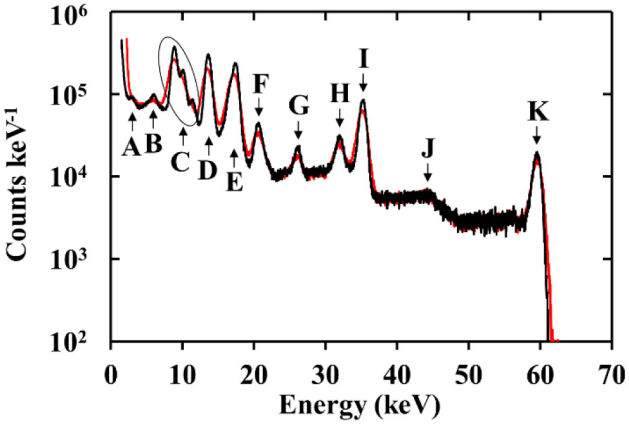

Fig. 18. ^{241}Am X-ray and γ-ray spectra obtained using the spectrometer pixel D9 at 100 °C (−100 V; 0.5 μs; 1.57 keV ± 0.08 keV FWHM at 59.54 keV; —) and at 20 °C (−100 V; 2 μs; 1.03 keV ± 0.08 keV FWHM at 59.54 keV; —). The major peaks identified are: (A) In Lβ detector fluorescence; (B) Cr Kα and Fe Kα capsule fluorescence; (C) Ga and As detector fluorescence and escape from ^{241}Am Np Lβ and Lγ X-ray photons; (D) ^{241}Am Np Lα; (E) ^{241}Am Np Lβ; (F) ^{241}Am Np Lγ; (G) ^{241}Am 26.3 keV γ-ray; (H) ^{241}Am 33.2 keV γ-ray; (I) In Kα escape from ^{241}Am 59.54 keV γ-rays and pulse pile up from Np Lβ X-ray photons; (J) ^{241}Am 43.4 keV γ-ray; (K) ^{241}Am 59.54 keV γ-ray.

was fitted to the γ-ray peak at 59.54 keV and its centroid channel number along with that of the noise peak at 0 keV were used to energy calibrate the MCA charge scale. The channel number of the low energy cut-off of the MCA was set to > 0 keV in order to limit the counts of the noise peak at 0 keV (e.g. 2.2 keV at 100 °C and 1.5 keV at 20 °C). All the characteristic emissions of the radioisotope ^{241}Am X-ray and γ-ray source [47,48], presented in Table 2, are apparent in Fig. 18. The 250 μm Be window of the source's capsule fully attenuated the α particles which would have otherwise been present.

In, Ga, and As fluorescence peaks (at 3.5 keV and from 9.2 keV to 11.7 keV) from the pixel, including its substrate, are also visible in the spectra shown in Fig. 18. Detector escape peaks were also apparent: Ga Kα and Kβ from Np Lβ and Lγ X-rays, As Kα and Kβ from Np Lγ X-rays, and In Kα from 59.54 keV γ-ray photons. The counts between ≈5.4 keV and ≈6.4 keV were attributed to the Cr Kα and Fe Kα fluorescence photons arising from the stainless steel capsule of the ^{241}Am radioisotope source. The FWHM at 59.54 keV improved as the temperature was reduced: FWHM at 59.54 keV of 1.57 keV ± 0.08 keV at 100 °C and 1.03 keV ± 0.08 keV at 20 °C were measured.

The ^{109}Cd X-ray and γ-ray spectra accumulated at the maximum (100 °C) and the minimum (20 °C) temperatures using D9 are shown

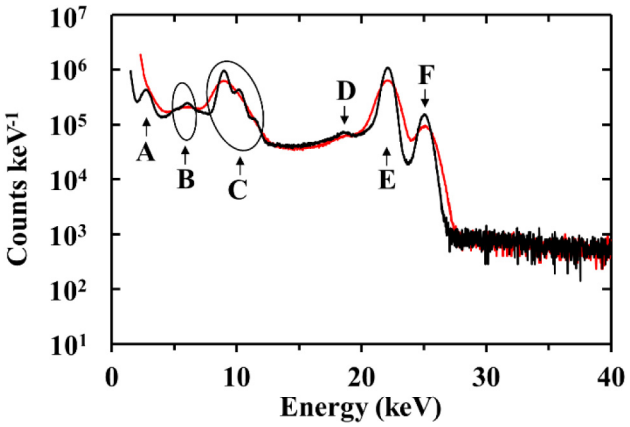

Fig. 19. ^{109}Cd X-ray and γ-ray spectra obtained with the spectrometer pixel D9 at 100 °C (−100 V; 0.5 μs; 1.58 keV ± 0.08 keV FWHM at 22.16 keV; —) and at 20 °C (−100 V; 2 μs; 0.94 keV ± 0.04 keV FWHM at 22.16 keV; —). The major peaks identified are: (A) ^{109}Cd Ag Lα; (B) Cr Kα and Fe Kα capsule fluorescence; (C) Ga and As detector fluorescence and escape from ^{109}Cd Ag Kα X-ray photons; (D) In Lβ escape from ^{109}Cd Ag Kα X-ray photons; (E) ^{109}Cd Ag $K\alpha_1$ and $K\alpha_2$ (combined); (F) ^{109}Cd Ag Kβ.

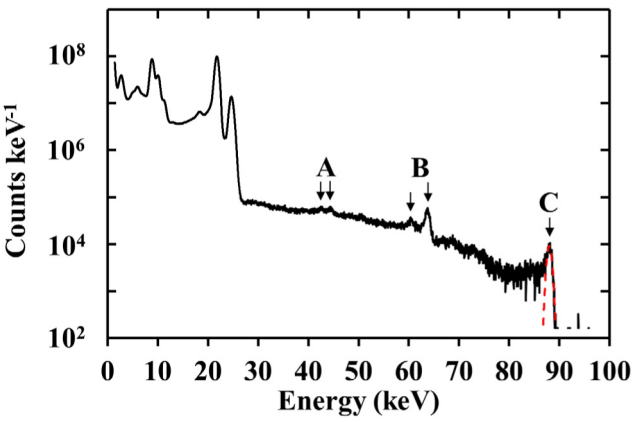

Fig. 20. ^{109}Cd X-ray and γ-ray spectrum obtained over a 72 h live time with the spectrometer pixel D9 at 20 °C (−100 V; 2 μs; 1.04 keV ± 0.08 keV FWHM at 88 keV; —), along with the fitted Gaussian at 88 keV (---). The major peaks identified, in addition to those shown in Fig. 19, are: (A) pulse pile up peaks from ^{109}Cd Ag Kα and Kβ X-ray photons; (B) In Kα and Kβ escape peaks from ^{109}Cd 88 keV γ-ray photons; (C) ^{109}Cd 88 keV γ-ray.

in Fig. 19. The combined Ag $K\alpha_1$ and Ag $K\alpha_2$ peaks were fitted with Gaussian peaks, taking into account the relative (Ag $K\alpha_2$; Ag $K\alpha_1$) radioisotope source's emission ratio and quantum detection efficiency of the pixels. The position (centroid channel number) of the Ag $K\alpha_1$ at 22.16 keV and of the noise peak at 0 keV were used to energy calibrate the MCA charge scale. The channel number of the low energy cut-off of the MCA was set to > 0 keV in order to eliminate the number of counts of the noise peak at 0 keV (e.g. 2.3 keV at 100 °C and 1.5 keV at 20 °C). Part of the main characteristic emission of the ^{109}Cd radioisotope X-ray and γ-ray source was the 88 keV γ-ray line [46]. However, even at full depletion, the *QE* of D9 at 88 keV was low (0.00256, see Fig. 2) and hence few 88 keV γ-ray photons were detected during the 8 h live time; as such for clarity the energy axis of the figure has been truncated at 40 keV in order to show better the peaks present in the spectra at energies below this.

All the main characteristic emission lines of the ^{109}Cd radioisotope X-ray and γ-ray source (Table 2), apart from the 88 keV γ-ray, are apparent in the spectra shown in Fig. 19. Ga and As detector fluorescence peaks (from 9.2 keV to 11.7 keV) are also visible in the spectra shown in Fig. 19. Ga, As, and In escape peaks (at 10.3 keV to 11.9 keV and at 18.5 keV) correspondent with Ag Kα X-rays are also visible. As was the case for the ^{241}Am X-ray and γ-ray spectra, fluorescence photons (Fe Kα at 6.4 keV; Cr Kα at 5.4 keV) of the stainless steel capsule of the source formed a combined peak, which is visible in Fig. 19. The energy resolution (FWHM at 22.16 keV) improved from 1.58 keV ± 0.08 keV to 0.94 keV ± 0.08 keV, as the temperature decreased from 100 °C to 20 °C. As a result, the Ag Kα and Ag Kβ photopeaks were less well resolved at 100 °C cf. that at 20 °C and the Ag Lα peak was not resolved from the zero energy noise peak at 100 °C (Fig. 19).

The 72 h live time ^{109}Cd X-ray and γ-ray spectrum obtained using D9 at 20 °C is shown in Fig. 20. In addition to the Ag Lα, Kα, and Kβ photopeaks which were also seen in Fig. 19, the 88 keV γ-ray peak is well formed in this long accumulation time spectrum. The FWHM at 88 keV was 1.04 keV ± 0.08 keV at 20 °C. The two peaks at ≈44 keV were attributed to pulse pile-up from pulses arising from the detection of Ag Kα and Kβ photons. Detector escape peaks, In Kα and Kβ from 88 keV γ-ray photons, are apparent in the spectrum.

A summary of the energy resolutions achieved as functions of photon energy (i.e. FWHM at 5.9 keV, 22.16 keV, 59.54 keV, and 88 keV) at 100 °C and 20 °C can be seen in Table 3. Incomplete charge collection noise varies as a function of photon energy [53]. The presence of incomplete charge collection noise at −100 V applied reverse bias was investigated by calculating the combined contribution (summed in quadrature) of the electronic noise and (if any) incomplete charge collection noise (i.e. total noise excluding only the energy dependent Fano noise) and observing its dependency upon the photon energy; this is also reported in Table 3. An energy dependent total noise excluding the Fano noise would suggest the presence of incomplete charge collection noise. However, an energy invariant (within uncertainties) remainder was calculated when the Fano noise was subtracted from the total noise. The absence of detectable incomplete charge collection noise across the energy range within the investigated temperatures when the detector was operated at −100 V applied reverse bias, was thus deduced from the results shown in Table 3.

The electronic noise contribution was inferred from the values in Table 3; it reduced from 1.53 keV ± 0.02 keV (rms error) (corresponding to 128 e^- rms ± 2 e^- rms) at 100 °C to 0.89 keV ± 0.02 keV (rms error) (corresponding to 71 e^- rms ± 2 e^- rms) at 20 °C.

The FWHM as a function of photon energy, presented in Table 3, was extracted from spectra accumulated with significantly different live times; a live time of 300 s was set for the ^{55}Fe X-ray spectra (extracted FWHM at 5.9 keV), whereas a live time of 8 h was set for the ^{241}Am X-ray and γ-ray spectra (extracted FWHM at 59.54 keV) and ^{109}Cd X-ray and γ-ray spectra (extracted FWHM at 22.16 keV), in addition to one additional ^{109}Cd X-ray and γ-ray spectrum with a live time limit of 72 h (extracted FWHM at 88 keV) accumulated at 20 °C. Relatively long spectrum accumulation times may cause gain drifts or charge accumulations, due to instrument instabilities, which may result in the broadening of the peaks and/or spectrum distortion [60]. The photon energy invariant remainder, within uncertainties, of the total noise when the Fano noise was subtracted (Table 3) suggested that no long-term instabilities were observed with the reported spectrometer up to a live accumulation time of 72 h compared to that potentially occurred within an accumulation live time of 300 s.

5. Summary and conclusions

A monolithic AlInP 3 × 3 pixel array detector was explored in photon counting X-ray and γ-ray spectroscopy, while it was operated (along with the preamplifier) uncooled at temperatures ≤100 °C. The AlInP structure was p^+-i-n^+ with a 6 μm thick i layer; each pixel of the array was a square mesa (200 μm × 200 μm).

Seven of the nine pixels showed similar leakage currents at 20 °C; they ranged from 0.97 pA ± 0.01 pA (D1) to 11.33 pA ± 0.06 pA (D3) at −200 V applied reverse bias. Exceptions were the pixels D5 and D7 which showed higher leakage currents (105.7 pA ± 0.5 pA at −70 V for

Table 3
The FWHM as a function of photon energy, achieved using the spectrometer pixel D9 at 100 °C and 20 °C. The extracted combined contribution (summed in quadrature) of the electronic and (if any) incomplete charge collection noise, is presented.

T (°C)	FWHM (keV) @				FWHM (keV) excl. Fano noise @			
	5.9 keV	22.16 keV	59.54 keV	88 keV	5.9 keV	22.16 keV	59.54 keV	88 keV
100	1.54 ± 0.08	1.58 ± 0.08	1.57 ± 0.08	–	1.53 ± 0.08	1.56 ± 0.08	1.51 ± 0.08	–
20	0.88 ± 0.04	0.94 ± 0.04	1.03 ± 0.08	1.04 ± 0.08	0.87 ± 0.04	0.90 ± 0.04	0.9 ± 0.1	0.9 ± 0.1

D5 and 320.5 pA ± 0.9 pA at −45 V for D7) compared to the rest of the pixels. At the greatest (in magnitude) investigated applied reverse bias (−200 V, corresponding to an electric field strength of 333 kV cm^{-1}), the leakage current of the packaged pixel D1, which was considered to be a representative pixel, reduced from 31.7 pA ± 0.2 pA at 100 °C to 0.99 pA ± 0.01 pA at 20 °C, whereas the leakage current density of the pixel D1 reduced from 27.3 nA cm^{-2} ± 0.1 nA cm^{-2} at 100 °C to 2.48 nA cm^{-2} ± 0.03 nA cm^{-2} at 20 °C. All pixels had the same capacitance. The effective carrier concentration within the i layer of pixel D1 at 20 °C had a minimum of 13×10^{14} cm^{-3} ± 3×10^{14} cm^{-3}; an applied reverse bias of −142 V was required for full depletion of the i layer.

The energy resolution (FWHM at 5.9 keV) achieved using each of the pixels was recorded at 20 °C; it improved when −50 V reverse bias was applied cf. that achieved at no applied bias, whereas no improvement was recorded for further increases up to and including the maximum (in magnitude) investigated applied reverse bias (−200 V). The FWHM at 5.9 keV ranged from 780 eV ± 40 eV (for D1, D3, and D4) to 810 eV ± 40 eV (for D5), with a mean value of 790 eV ± 10 eV (rms error) for all pixels apart from D7, suggesting that all pixels except one had the same energy resolution at 20 °C; the exception was pixel D7, which had 1000 eV ± 40 eV FWHM at 5.9 keV, due to its relatively high leakage current.

The spectroscopic response of one pixel, D1, was investigated comprehensively across temperatures from 100 °C to 20 °C. The best energy resolution (FWHM at 5.9 keV) achieved with D1 improved from 1.49 keV ± 0.06 keV to 0.82 keV ± 0.04 keV, as the temperature decreased from 100 °C to 20 °C. As was the case at 20 °C, its FWHM at each temperature improved at −50 V applied reverse bias, cf. that achieved at no applied bias, and then stabilized (within uncertainties) for applied reverse bias increases up to and including −200 V. Noise analysis suggested that the optimum shaping time was 0.8 μs at 100 °C and 2.8 μs at 20 °C; the optimum available shaping time on the shaping amplifier employed in the experiments was determined to be 0.5 μs at 100 °C and between 2 μs and 3 μs at 20 °C. The noise with the highest contribution to the peak broadening at 100 °C was the dielectric noise for $\tau \leq$ 4 μs, whereas the white parallel noise dominated for $\tau >$ 4 μs. The dielectric noise reduced from 104 e^- rms at 100 °C to 64 e^- rms at 40 °C and 20 °C. The AlInP spectrometer had better energy resolution than a similar GaAs spectrometer [12] at 100 °C, whereas the opposite was the case at temperatures ≤80 °C, even though both spectrometers had similar equivalent noise charge at 20 °C.

Pixel D9, which was on the corner diagonally opposite D1, was investigated across the same temperature range and with ^{55}Fe X-ray, ^{109}Cd X-ray and γ-ray, and ^{241}Am X-ray and γ-ray radioisotope sources, thus providing a range of 5.9 keV to 88 keV photon energies. The energy resolution of the spectrometer at 100 °C was 1.54 keV FWHM at 5.9 keV, 1.58 keV FWHM at 22.16 keV, and 1.57 keV FWHM at 59.54 keV; the uncertainty associated with the FWHM was 0.08 keV in each case. At 20 °C, the FWHM were 0.88 keV ± 0.04 keV (at 5.9 keV), 0.94 keV ± 0.08 keV (at 22.16 keV), 1.03 keV ± 0.08 keV (at 59.54 keV), and 1.04 keV ± 0.08 keV (at 88 keV).

The presence of incomplete charge collection noise arising from charge trapping and recombination was explored using three methods. For temperatures ≤80 °C, no evidence of incomplete charge collection noise was found when the pixels were operated at −50 V, −100 V, and −200 V. However, an applied reverse bias of −100 V was required to ensure the absence of incomplete charge collection at the maximum investigated temperature (100 °C).

The results demonstrate a small mesa AlInP pixel photodiode array for the first time. The array has promising characteristics which, if replicated in arrays with greater numbers of pixels, would be valuable for spectroscopic X-ray and γ-ray imaging. The array was found to be suitable for photon counting X-ray and γ-ray spectroscopy; it operated uncooled at temperatures ≤100 °C. The limiting factor of the energy resolution of the spectrometer was the lossy dielectrics at the input of the preamplifier; this finding highlights the need to redesign the preamplifier front-end in order to reduce the parasitic dielectrics and achieve better performance. The work shows that AlInP material technology has reached sufficient maturity that small pixel arrays can be produced with broadly uniform performance, paving the way towards the production of monolithic AlInP arrays with greater number of pixels that can operate in high temperature environments without cooling. Although crosstalk between pixels – which is an important characteristic of pixel arrays – was not investigated here, in future work, arrays with larger numbers of pixels shall be reported, while also studying their inter-pixel crosstalk. It is planned to investigate the crosstalk effects in future through the development of custom Monte Carlo codes and through experimental work at synchrotron facilities using micro focus (∼μm diameters) X-ray beams which can be used to scan each of the pixels individually – and indeed the areas between the pixels – to characterize the response of the detector array in this regard.

CRediT authorship contribution statement

G. Lioliou: Conceptualization, Methodology, Validation, Formal analysis, Investigation, Data curation, Writing - original draft, Writing - review & editing, Visualization. **A.B. Krysa:** Conceptualization, Software, Investigation, Resources, Data curation, Writing - review & editing. **A.M. Barnett:** Conceptualization, Methodology, Validation, Formal analysis, Investigation, Resources, Data curation, Writing - original draft, Writing - review & editing, Visualization, Supervision, Project administration, Funding acquisition.

Declaration of competing interest

The authors declare that they have no known competing financial interests or personal relationships that could have appeared to influence the work reported in this paper.

Acknowledgements

This work was in part supported by the Science and Technology Facilities Council, United Kingdom, through grants ST/P001815/1 and ST/R001804/1 and the Engineering and Physical Sciences Research Council, United Kingdom, through grant EP/P021271/1 (University of Sussex, A.M.B., PI). A.M.B. acknowledges funding from The Leverhulme Trust, United Kingdom, in the form of a 2016 Philip Leverhulme Prize. The authors acknowledge N.R. Gemmell for contributions to MATLAB programming. The authors acknowledge R.J. Airey and S. Kumar, EPSRC National Epitaxy Facility, for device fabrication. All data that support the findings of this study are included within the article.

References

[1] D. Barret, et al., Proc. SPIE 9905 (2016) 99052F.
[2] J. Benkhoff, J. van Casteren, H. Hayakawa, M. Fujimoto, H. Laakso, M. Novara, P. Ferri, H.R. Middleton, R. Ziethe, Planet. Space Sci. 58 (2010) 2.
[3] K. Taguchi, J.S. Iwanczyk, Med. Phys. 40 (2013) 100901.
[4] V. Rebuffel, J. Rinkel, J. Tabary, L. Verger, International Symposium on Digital Industrial Radiology and Computed Tomography, Berlin, 2011.
[5] M.J. Pushie, I.J. Pickering, M. Korbas, M.J. Hackett, G.N. George, Chem. Rev. 114 (2014) 8499.
[6] Y. Kanemaru, et al., J. Instrum. 14 (2019) C04003.
[7] N. Meidinger, J. Eder, T. Eraerds, K. Nandra, D. Pietschner, M. Plattner, A. Rau, R. Strecker, Proc. SPIE 9905 (2016) 99052A.
[8] A.F. Abbey, P.J. Bennie, M.J.L. Turner, Altieri. B, S. Rives, Nucl. Instrum. Methods Phys. Res. A 513 (2003) 136.
[9] D. Blake, et al., Space Sci. Rev. 170 (2012) 341.
[10] M. Sammartini, M. Gandola, F. Mele, B. Garavelli, D. Macera, Pozzi. P, G. Bertuccio, Nucl. Instrum. Methods Phys. Res. A 910 (2018) 168.
[11] P. Kostamo, S. Nenonen, S. Vähänen, L. Tlustos, C. Fröjdh, M. Campbell, Y. Zhilyaev, H. Lipsanen, Nucl. Instrum. Methods Phys. Res. A 591 (2008) 174.
[12] G. Lioliou, A.M. Barnett, Nucl. Instrum. Methods Phys. Res. A 985 (2021) 164672.
[13] J.H. Hubbell, S.M. Seltzer, Tables of X-ray Mass Attenuation Coefficients and Mass Energy- Absorption Coefficients (Version 1.4), National Institute of Standards and Technology, Gaithersburg, 2004.
[14] S.M. Sze, K.K. Ng, Physics of Semiconductor Devices, John Wiley & Sons, New Jersey, 2007.
[15] W. Bludau, A. Onton, W. Heinke, J. Appl. Phys. 45 (1974) 1846.
[16] S. De Sordo, L. Abbene, E. Caroli, A.M. Mancini, A. Zappettini, P. Ubertini, Sensors 9 (2009) 3491.
[17] G. Bertuccio, D. Maiocchi, J. Appl. Phys. 92 (2002) 1248.
[18] M. Mahdavi, K.L. Giboni, S. Vajda, J.S. Schweitzer, J.A. Truax, First Year PIDDP Report On Gamma-Ray and X-ray Spectroscopy X-ray Remote Sensing and in Situ Spectroscopy for Planetary Exploration Missions NASA. document ID 19950009501.
[19] S. Butera, T. Gohil, G. Lioliou, A. B, A.M. Barnett, J. Appl. Phys. 120 (2016) 174503.
[20] G. Lioliou, A.B. Krysa, A.M. Barnett, J. Appl. Phys. 124 (2018) 195704.
[21] G. Bertuccio, S. Caccia, D. Puglisi, D. Macera, Nucl. Instrum. Methods Phys. Res. A 652 (2011) 193.
[22] C.S. Bodie, G. Lioliou, G. Lefeuvre, A.M. Barnett, Nucl. Instrum. Methods Phys. Res. A 991 (2021) 165025.
[23] A. Auckloo, J.S. Cheong, X. Meng, C.H. Tan, J.S. Ng, A.B. Krysa, R.C. Tozer, J.P.R. David, J. Instrum. 11 (P03021) (2016).
[24] S. Butera, G. Lioliou, A.B. Krysa, A.M. Barnett, J. Appl. Phys. 120 (2016) 024502.
[25] J.S. Cheong, J.S. Ong, J.S. Ng, A.B. Krysa, J.P.R. David, IEEE J. Sel. Top. Quantum Electron. 20 (2014) 142.
[26] S. Zhao, S. Butera, G. Lioliou, A.B. Krysa, A.M. Barnett, Sci. Rep. 9 (2019) 12155.
[27] G. Lioliou, S. Butera, A.B. Krysa, A.M. Barnett, Nucl. Instrum. Methods Phys. Res. A 943 (2019) 162467.
[28] S. Zhao, G. Lioliou, S. Butera, A.B. Krysa, A.M. Barnett, Nucl. Instrum. Methods Phys. Res. A 960 (2020) 163606.
[29] R. Van Grieken, Markowicz, A Handbook of X-Ray Spectrometry, Marcel Dekker, New York, 2002.
[30] R. Jenkins, Quantitative X-Ray Spectrometry, Marcel Dekker, New York, 1995.
[31] Temperature Applied Sciences Ltd, Goring Business Park, Goring-by-Sea, West Sussex, BN12 4HF, England, UK.
[32] Keysight Technologies, 2019. B2980 Series Femto/Picoammeter Electrometer/High Resistance Meter, B2980-90010 (Tokyo: Keysight Technologies).
[33] Keithley Instruments 2013 Series 2600B System SourceMeter®Instrument Reference Manual, 2600BS-901-01 Rev. B (Ohio: Keithley Instruments).
[34] G. Lioliou, M.D.C. Whitaker, A.M. Barnett, J. Appl. Phys. 122 (2017) 244506.
[35] G. Bertuccio, D. Puglisi, D. Macera, R.Di. Liberto, Lamborizio. M, L. Mantovani, IEEE Trans. Nucl. Sci. 61 (2014) 961.
[36] Hewlett Packard, Model HP 4275A Multi-Frequency LCR Meter Operating Manual, 04275-90004, Hewlett Packard, Tokyo, 1979.
[37] Keithley Instruments 2011 Model 6487 Picoammeter/Voltage Source Reference Manual, 6487-901-01 Rev C (Ohio: Keithley Instruments).
[38] Y. Nishikawa, M. Suzuki, M. Okajima, Jpn. J. Appl. Phys. 32 (1993) 498.
[39] M. Kondo, N. Okada, K. Domen, K. Sugiura, C. Anayama, T. Tanahashi, J. Electron. Mater. 23 (1994) 355.
[40] K.A. Bertness, S.R. Kurtz, S.E. Asher, R.C. Reedy Jr, J. Cryst. Growth 196 (1999) 13.
[41] G. Bertuccio, P. Rehak, D. Xi, Nucl. Instrum. Methods Phys. Res. A 326 (1993) 71.
[42] InterFET Corporation 2004 Semiconductor Databook, 4(6) (Garland: InterFET Corporation).
[43] ORTEC 2004 Model 572A Spectroscopy Amplifier Operating and Service Manual, 0904 Rev. D (Oak Ridge: Advanced Measurement Technology, Inc.).
[44] ORTEC 2014 EASY-MCA-8K™EASY-MCA-2K™ Digital Gamma-Ray Spectrometer User's Manual, 1014 Rev. C (Oak Ridge: Advanced Measurement Technology, Inc.).
[45] U. Schötzig, Appl. Radiat. Isot. 53 (2000) 469.
[46] H. Xiaolong, Y. Shenggui, D. Chunsheng, Nucl. Instrum. Methods Phys. Res. A 621 (2010) 443.
[47] H.R. Verma, Appl. Radiat. Isot. 122 (2017) 41.
[48] M.-M. Be, V. Chiste, C. Dulieu, X. Mougeot, E. Browne, V. Chechev, N. Kuzmenko, F. Kondev, A. Luca, M. Galan, A.L. Nichols, A. Arinc, X. Huang, Table of Radionuclides ($A = 22$ to $A = 244$), Bureau International des Poids et Mesures, Sèvres, 2010.
[49] S. Zhao, S. Butera, G. Lioliou, A.B. Krysa, A.M. Barnett, J. Phys. D 52 (2019) 225101.
[50] G. Lutz, J. Synchrotron Radiat. 13 (2006) 99.
[51] Lioliou. G, A.M. Barnett, Nucl. Instrum. Methods Phys. Res. A 801 (2015) 63.
[52] U. Fano, Phys. Rev. 72 (1947) 26.
[53] Owens. A, A. Peacock, Nucl. Instrum. Methods Phys. Res. A 531 (2004) 18.
[54] Bertuccio. G, A. Pullia, Rev. Sci. Instrum. 64 (1993) 3294.
[55] S. Butera, G. Lioliou, Krysa.A. B, A.M. Barnett, Nucl. Instrum. Methods Phys. Res. A 879 (2017) 64.
[56] G. Bertuccio, Canali. C, F. Nava, Nucl. Instrum. Methods Phys. Res. A 410 (1998) 29.
[57] M. Tsubota, J.H. Kaneko, D. Miyazaki, T. Shimaoka, K. Ueno, T. Tadokoro, A. Chayahara, H. Watanabe, Y. Kato, S.I. Shikata, H. Kuwabara, Nucl. Instrum. Methods Phys. Res. A 789 (2015) 50.
[58] G. Bertuccio, R. Casiraghi, IEEE Trans. Nucl. Sci. 50 (2003) 175.
[59] G. Bertuccio, A. Pullia, G. De Geronimo, Nucl. Instrum. Methods Phys. Res. A 380 (1996) 30.
[60] G.F. Knoll, Radiation Detection and Measurement, John Wiley & Sons, New Jersey, 2010.